Ceramics International 43 (2017) 8276–8283

Contents lists available at ScienceDirect

Ceramics International

journal homepage: www.elsevier.com/locate/ceramint

Tunable photoluminescence of nanostructured $LaPO_4:Eu^{3+}/Tb^{3+}$ synthesized via a microwave-assisted ethylene glycol route

R.S. de Oliveira[a], B.S. de Brito[a], J. Kulesza[b], S. Alves-Jr[b], B.S. Barros[c,*]

[a] Institute of Chemistry, Federal University of Rio Grande do Norte, Campus Universitário Lagoa Nova, 59072-970, Natal, RN, Brazil
[b] Department of Fundamental Chemistry, Federal University of Pernambuco, Av. Prof. Moraes Rego, 1235 - Cidade Universitária, 50670-901, Recife, PE, Brazil
[c] Department of Mechanical Engineering, Federal University of Pernambuco, Av. Prof. Moraes Rego, 1235 - Cidade Universitária, 50670-901, Recife, PE, Brazil

ARTICLE INFO

Keywords:
Photoluminescence
Lanthanum phosphate
Lanthanides
Ethylene glycol
Microwaves

ABSTRACT

Nanostructured phosphors $LaPO_4:Eu^{3+}/Tb^{3+}$ were prepared via a combined approach using microwave heating and a bifunctional solvent (ethylene glycol) acting as both microwave absorber and capping agent. The synthesized samples were characterized by X-ray diffraction (XRD), attenuated total reflectance Fourier transform infrared spectroscopy (ATR-FTIR), transmission electron microscopy (TEM) and photoluminescence (PL) measurements. All samples crystallized in a monoclinic monazite-type structure. Electron microscopy analysis revealed a hierarchical organization of self-assembled seed crystals of lanthanum phosphate into nanoparticles that, in turn, gave rise to sponge-like aggregates. The co-doped samples exhibited self-activated blue luminescence from the host matrix, as well as red and green emissions due to the presence of Eu^{3+} and Tb^{3+} ions, respectively. Furthermore, the spectroscopic analysis indicated energy transfer from terbium to europium ions.

The synthetic route described here is efficient to prepare nanomaterials with advanced optical properties, which exhibit a potential for applications in photonics, sensing and biolabelling.

1. Introduction

Lanthanide-based luminescent materials have attracted much attention in the last decades, particularly in the field of biomedicine, where they have been used as biomarkers [1,2]. The use of lanthanides in biomarker materials is especially attractive due to their unique spectroscopic properties, such as long-living luminescence, large Stokes shifts and narrow high-intensity emission bands due to their 4f-5d and 4f-4f electronic transitions [3,4].

Among various materials, nanostructured oxides have frequently been reported as good host matrices for lanthanide ions, acting as activators and conferring luminescent properties to these materials [4–12]. Lanthanide-doped phosphate nanomaterials have shown interesting luminescent properties and biocompatibility - two crucial issues that should be considered for biological and medical applications [13,14].

In particular, lanthanum phosphate ($LaPO_4$) has been described as a suitable host matrix for lanthanide ions, such as Eu^{3+} and Tb^{3+}, among others [3,15–17]. Also, the co-doping approach can be used to prepare compounds with tunable and multicolor emission [15,16]. Nevertheless, some important factors such as particle size, morphology, and state of agglomeration, may affect the luminescent properties or even limit their biomedical applications [18,19]. The most frequently reported methods for the preparation of $LaPO_4$ doped with different lanthanide ions are the solid-state reactions [20], wet-chemical synthesis [21], sol-gel [22], self-combustion [23] and hydrothermal method [24]. However, those methods are often inefficient in controlling the morphology and the particle size of obtained materials.

Microwave-assisted solvothermal synthesis in ethylene glycol is a fast and quite simple alternative for the preparation of nanoscale materials, including lanthanides-doped metal phosphates. This synthetic route is particularly attractive due to the double function of ethylene glycol, which acts as both a solvent and a capping agent, preventing the particle growth [25–28].

The aim of this study was to synthesize nanostructured materials displaying tunable photoluminescence properties dependent on the dopant concentration and excitation wavelength. The results demonstrate the effectiveness of microwave irradiation and ethylene glycol (EG) in the particle growth control.

Furthermore, such nanostructured materials exhibit a set of proper-

* Corresponding author.
E-mail address: braulio.barros@ufpe.br (B.S. Barros).

http://dx.doi.org/10.1016/j.ceramint.2017.03.160
Received 15 February 2017; Received in revised form 22 March 2017; Accepted 25 March 2017
Available online 27 March 2017

ties required for application as biomarkers.

2. Material and methods

The reagents: $La(NO_3)_3.6H_2O$ (Vetec, 99%), Tb_4O_7 (Sigma-Aldrich, > 99%), Eu_2O_3 (Sigma-Aldrich, > 99%), Na_2HPO_4 (ProQuímicos, 99%), NaOH (ProQuímicos, 97%), and ethylene glycol, EG (Vetec, 99.5%) were used as raw materials without further purification.

Nanocrystalline lanthanum phosphates were synthesized by a microwave-assisted solvothermal method using ethylene glycol as both solvent and capping agent. The adapted synthesis procedure is a modified version of that described by Patra et al. [29]. The procedure to obtain the co-doped sample $La_{0.93}Eu_{0.011}Tb_{0.059}PO_4$ was as follows: in a beaker, 11 mg (0.0147 mmol) of Tb_4O_7 and 1.9 mg (0.0055 mmol) of Eu_2O_3 were treated with the mixture of 4 mL of HNO_3 and 6 mL of H_2O at 90 °C and kept under stirring until complete solvent evaporation. Then, to the beaker containing generated in situ europium and terbium nitrates, 402.6 mg (0.93 mmol) of $La(NO_3)_3.6H_2O$ in 11 mL of EG were added, and the reaction mixture was stirred for 10 min at room temperature. Subsequently, 142 mg (1 mmol) of Na_2HPO_4 and 40 mg (1 mmol) of NaOH were added. Next, the precursor solution was sealed in a Teflon reactor and exposed to microwave irradiation in a commercial oven (Panasonic model NN-S62BK, 2.45 GHz, 1000 W). Syntheses were performed using 10% of maximum oven power for 10 min, reaching at the end the temperature of reaction of 140 °C. After cooling down to room temperature, the precipitate was collected by filtration, washed with ethanol five times and then dried in an oven at 70 °C for 10 min. Six samples with the following compositions: $LaPO_4$, $La_{0.93}Eu_{0.07}PO_4$, $La_{0.93}Tb_{0.07}PO_4$, $La_{0.93}Eu_{0.006}Tb_{0.064}PO_4$, $La_{0.93}Eu_{0.011}Tb_{0.059}PO_4$, $La_{0.93}Eu_{0.017}Tb_{0.053}PO_4$ were prepared using the appropriate amount of reagents.

The as-prepared powders were characterized by X-ray diffraction (XRD) on a diffractometer SHIMADZU model XRD-6000, using Cu Kα radiation and operating at 40 kV and 30 mA. The powder diffraction patterns were recorded between 10 and 80° at steps of 0.02°. The microstructure analysis was performed by scanning electron microscopy (SEM) using a microscope Hitachi Tabletop model TM300.

The transmission electron microscopy (TEM) was performed on a Tecnai 20 electron microscope with an acceleration voltage of 200 kV.

The attenuated total reflectance Fourier transform infrared spectroscopy (ATR-FTIR) experiments were carried out on a Bruker Vertex 70/v spectrometer. Photoluminescence (PL) excitation and emission spectra were collected at 293 K on a Fluorolog Horiba Jobin Yvon spectrofluorometer.

3. Results and discussion

As outlined in the introduction, the microwave-assisted solvothermal method, using ethylene glycol as both solvent and a capping agent, may be efficient in the preparation of nanostructured lanthanide/phosphate-based materials.

Fig. 1 shows the powder diffraction patterns of pure and doped lanthanum phosphates, as well as simulated pattern generated from the CIF file COD no 9001647 [30]. The CIF file corresponds to the $LaPO_4$ crystallized in the monazite-type structure with a monoclinic unit cell, space group *P*21/*c*. As can be seen from Fig. 1, the experimental and simulated patterns are in good agreement. However, diffraction peaks present significant broadening, suggesting small average crystallite size and/or relatively low crystallinity.

The effects of the reaction time and post-calcination on the particle size and shape were investigated. The samples synthesized within the reaction time of 10, 20, 40 and 60 min present very similar X-ray diffraction patterns with broad peaks (Fig. 2a–b). We assume that the reaction time has a little effect on the particle growth and, as expected, the small particle size may be attributed to the use of ethylene glycol as a capping agent. The samples prepared within 10 min and calcined at

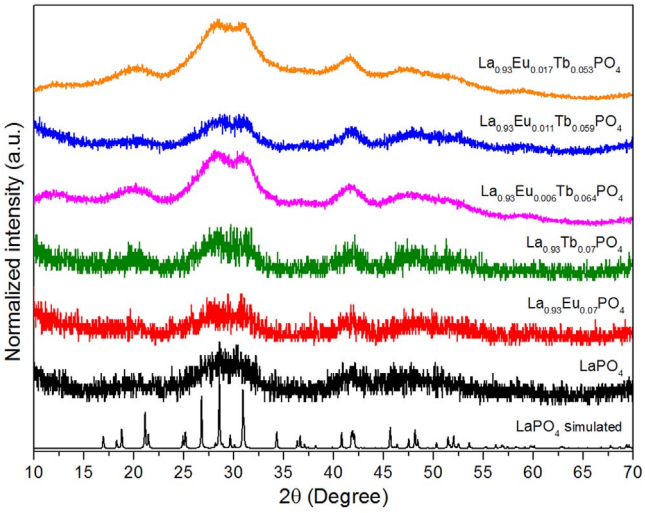

Fig. 1. X-ray diffraction patterns of the as-synthesized samples compared to the simulated $LaPO_4$ pattern.

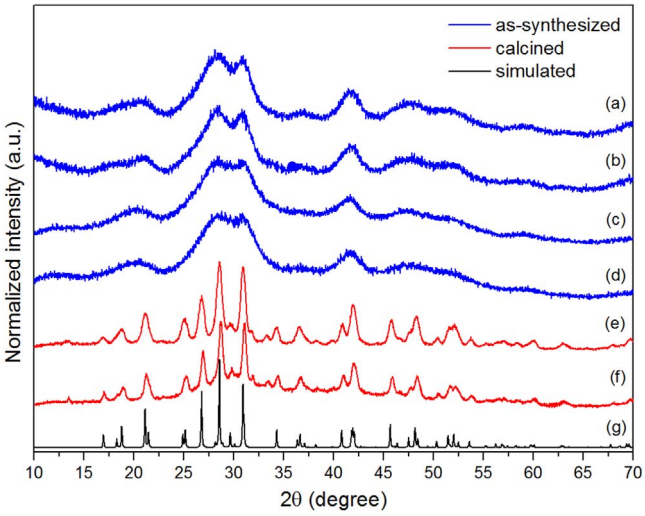

Fig. 2. X-ray diffraction patterns of $La_{0.93}Eu_{0.006}Tb_{0.064}PO_4$ synthesized within reaction times of (a) 60 min, (b) 40 min, (c) 20 min, (d) 10 min, synthesized within reaction a time of 10 min and further calcined for (e) 30 min and (f) 120 min, and (g) simulated pattern of $LaPO_4$.

600 °C for 30 and 120 min exhibit narrow diffraction peaks, suggesting the decomposition of the capping agent, thus allowing the particle growth independently on the time of reaction (Fig. 2c–d).

TEM images and size distribution histograms of as-synthesized and calcined samples are shown in Fig. 3. The as-synthesized sample presents two distinct nanocrystalline morphologies (Fig. 3a). In the region bounded by a white line, aggregates of seed crystals of $LaPO_4$ can be observed; whereas arrows indicate nanoparticles of $LaPO_4$ as a secondary monocrystalline morphology. Fig. 3b shows the nanoparticle size distribution for this sample with an average of 20 nm. This histogram was constructed on the basis of several images with the total count of 167 nanoparticles, ignoring the seed crystal regions.

Despite the impossibility of measuring the seed crystal sizes based on these images, it seems that they are significantly smaller than nanoparticles, what may explain peak broadening in the XRD patterns.

Fig. 3c shows TEM image of the as-synthesized sample after calcination at 600 °C for 120 min. Comparing Fig. 3a and c, there is no apparent difference in the size and shape of nanoparticles. The nanoparticle size distribution for this sample presented an average of 24 nm (Fig. 3d). The histogram was built by analyzing several images with the total count of 344 nanoparticles. It is worth noting the

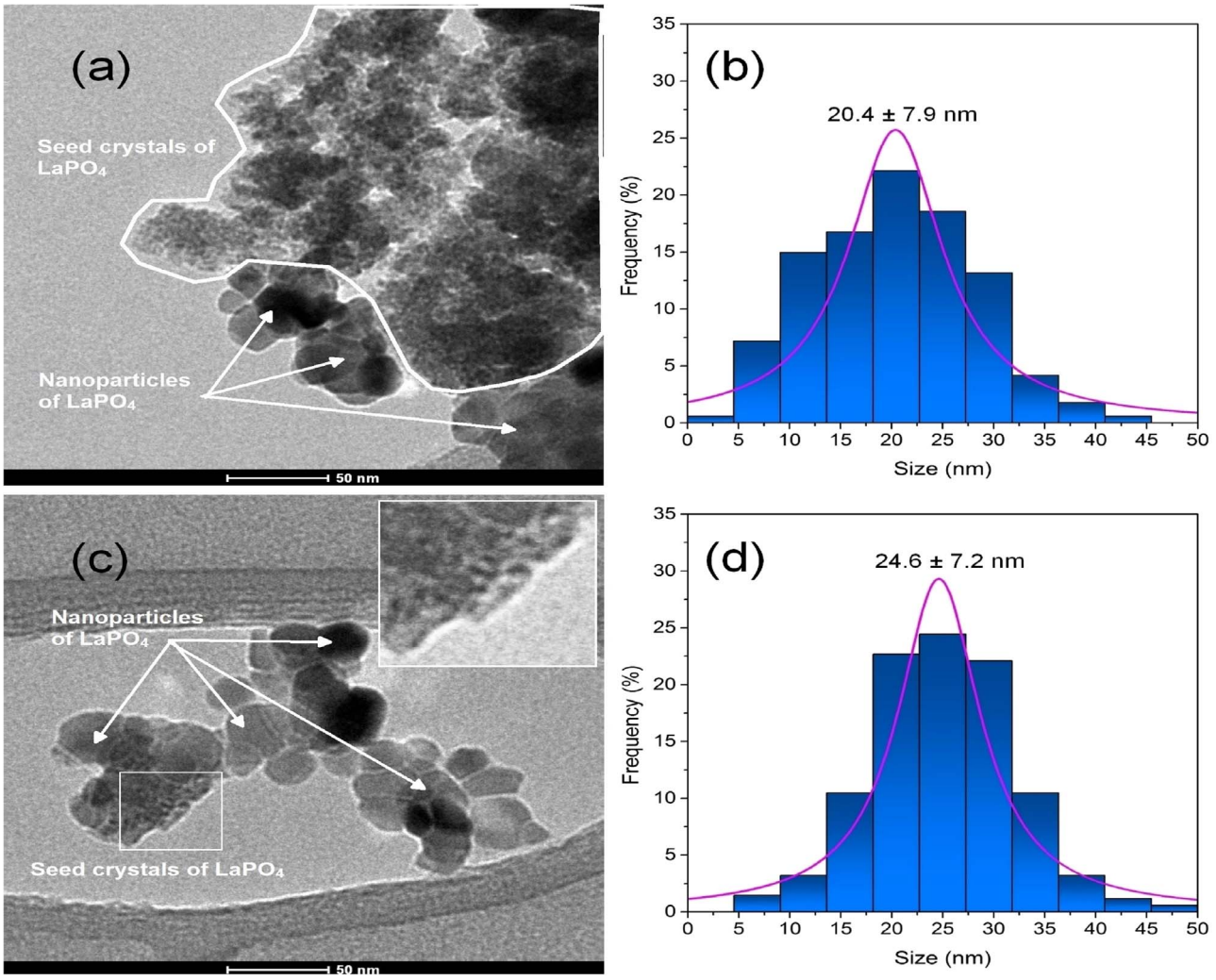

Fig. 3. TEM micrographs (left) and histograms showing nanoparticles size distribution (right) of $La_{0.93}Eu_{0.006}Tb_{0.064}PO_4$; as-prepared sample (a–b), calcined sample (c–d).

presence of traces of seed crystals in this sample (see the inset in Fig. 3c).

These results suggest the rapid nucleation of seed crystals, which posteriorly self-assemble to form aggregates. It is well known that the particle aggregation provides lower surface energy in a solvent, and it is characteristic for small particles, including seed crystals [31]. Seed crystals in an aggregate also tend to rotate and contact with their neighbors by sharing the same facet in a process known as Oriented Attachment (OA) [31,32]. The oriented seed crystal aggregates can be regarded as mesocrystals, and they diffract as single-crystals [31,33,34].

However, the diffraction patterns revealed in Fig. 1 show extremely broad peaks, suggesting that the seed crystals are not oriented in those aggregates. Apparently, the reaction time of 10 min is not enough to orientate the seed crystals (Fig. 3a). Furthermore, the post-calcination step promotes the formation of $LaPO_4$ nanospheres through coalescence and recrystallization of the seed crystals.

The ATR-FTIR spectra of the obtained powders are represented in Fig. 4. The spectra show a sharp band at around 1000 cm^{-1} with a shoulder band at 950 cm^{-1} which are assigned to the P-O symmetric stretching vibrations. Four bands observed at 532, 556, 573 and 613 cm^{-1} can be attributed to the asymmetric bending vibrations of O-P-O bonds [17,35,36]. This spectrum is consistent with the C_1 site symmetry of PO_4^{3-} anion in the monoclinic $LaPO_4$ structure according to Hezel and Ross [37].

Bands corresponding to solvent molecules H_2O and EG may also be

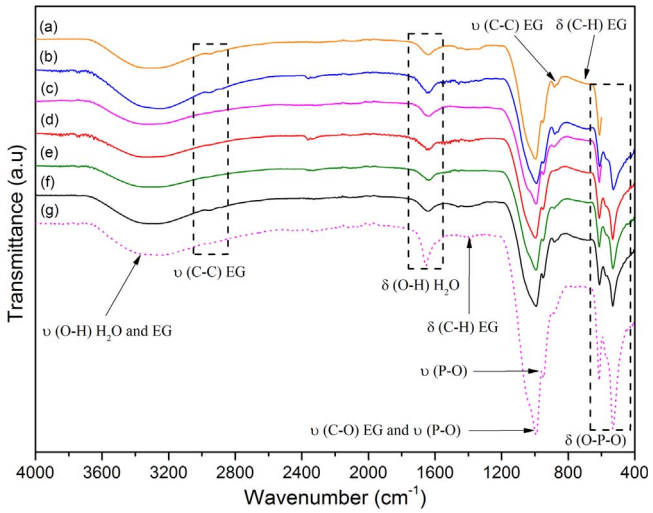

Fig. 4. ATR-FTIR spectra of the samples (a) $La_{0.93}Eu_{0.017}Tb_{0.053}PO_4$, (b) $La_{0.93}Eu_{0.011}Tb_{0.059}PO_4$, (c) $La_{0.93}Eu_{0.006}Tb_{0.064}PO_4$, (d) $La_{0.93}Tb_{0.07}PO_4$, (e) $La_{0.93}Eu_{0.07}PO_4$, (f) $LaPO_4$ as-synthesized and (g) $La_{0.93}Eu_{0.006}Tb_{0.064}PO_4$ dried at 90 °C for two hours.

visible in the IR spectra of all prepared samples. A broad band at around 3300 cm^{-1} and 1636 cm^{-1} can be attributed, respectively, to the stretching and bending vibrations of O-H group, indicating the

presence of coordinated water molecules in all samples [24,37]. However, bands corresponding to alcohol O-H group may also occur in the region of a spectrum around 3300 cm^{-1} overlapping bands of water O-H bonds.

It is well known that liquid water has three normal vibration modes at 3490, 3280 and 1644 cm^{-1}, corresponding to asymmetric stretching, symmetric stretching, and bending of the O–H bonds, respectively. The peaks are significantly shifted in comparison to the bands of vapor water due to the presence of hydrogen bonds between molecules in a liquid state. The main stretching bands in liquid water are shifted to lower wavenumbers (from 3756 to 3490 cm^{-1} and from 3652 to 3280 cm^{-1}, respectively), whereas the bending band wavenumber increases (from 1595 to 1644 cm^{-1}) [38,39]. In the IR spectra of prepared samples, those bands are slightly shifted to lower wavenumbers (3346, 3251 and 1641 cm^{-1}, respectively) in comparison to the literature data for liquid water. This observation may indicate that water molecules are coordinated in the structure of prepared samples.

The bands at around 2953 and 2880 cm^{-1} can be related to the stretching, asymmetric and symmetric C-H vibrations of the alkyl groups of the ethylene glycol (EG) used as a solvent in the synthesis. The corresponding bending vibrations of the C-H groups of EG may be observed at around 1450 and 725 cm^{-1}. A band at around 885 cm^{-1} may be attributed to the stretching C-C vibration of ethylene glycol, confirming the presence of the solvent in all samples [40]. The band corresponding to the stretching vibration of the C–O alcohol bond that usually occurs in a spectrum region between 1260 and 1050 cm^{-1} is not clearly visible here due to the superposition of bands of phosphate groups.

The band at 2356 cm^{-1} may correspond to the asymmetric stretching vibration of CO_2 probably adsorbed from the air. The bending vibration normally observed at around 666 cm^{-1} is not visible here, due to the superposition of bands from EG and phosphates.

SEM micrographs of the as-synthesized samples are shown in Fig. 5a–d. The images reveal soft porous agglomerates of small particles with a sponge-like microstructure. Apparently, both doped and undoped samples show the same kind of microstructure. It seems that the presence of lanthanide cations did not affect the microstructure of the prepared powders.

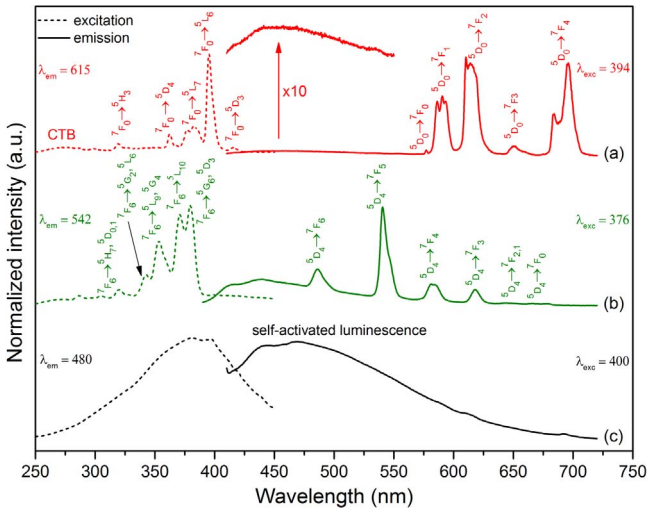

Fig. 6. PL excitation and emission spectra of $La_{0.93}Eu_{0.07}PO_4$ (a), $La_{0.93}Tb_{0.07}PO_4$ (b) and $LaPO_4$ (c).

Fig. 6 shows the excitation and emission spectra of $LaPO_4$, $La_{0.93}Eu_{0.07}PO_4$ and $La_{0.93}Tb_{0.07}PO_4$ recorded in the solid state at room temperature.

The excitation spectrum of $La_{0.93}Eu_{0.07}PO_4$ acquired by monitoring emission at 615 nm is depicted in Fig. 6a (dashed line). Sharp peaks can be easily identified with the most intense one at 394 nm assigned to the $^7F_0 \rightarrow {}^5L_6$ transition of Eu^{3+}. Furthermore, this spectrum also exhibits two broad bands of low intensity. The first one, with a

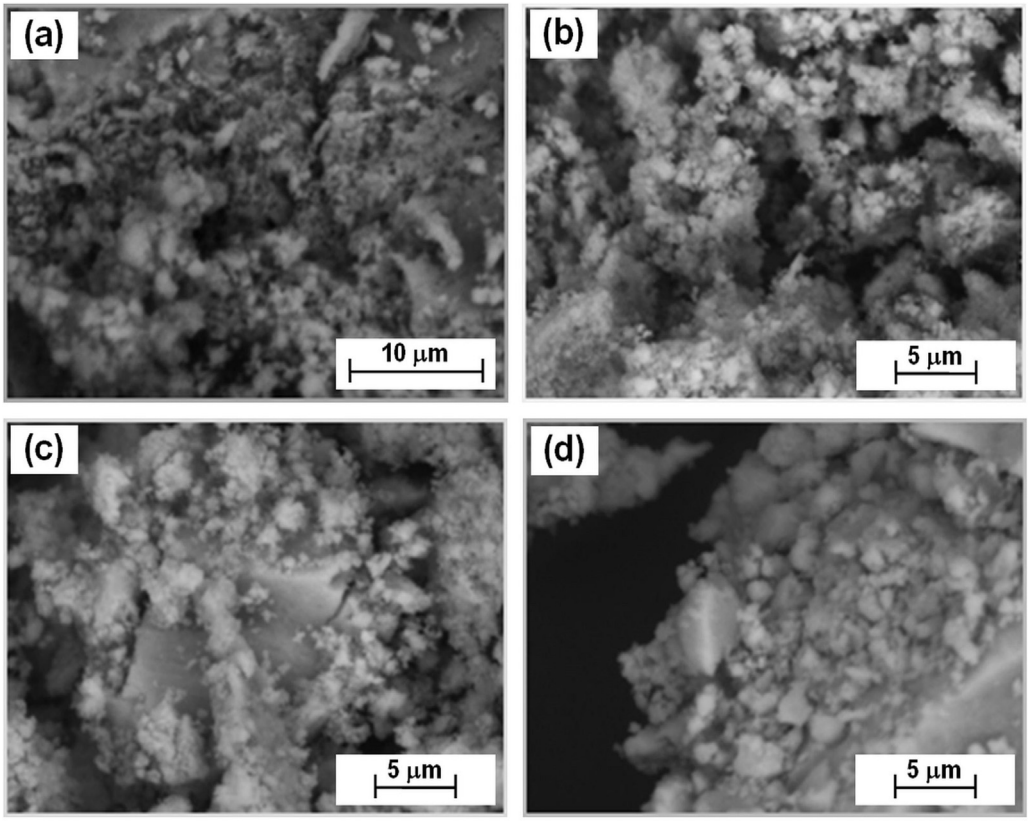

Fig. 5. SEM micrographs of the as-synthesized (a) $LaPO_4$, (b) $La_{0.93}Eu_{0.07}PO_4$, (c) $La_{0.93}Tb_{0.07}PO_4$ and (d) $La_{0.93}Eu_{0.011}Tb_{0.059}PO_4$.

maximum at 273 nm, is attributed to the charge-transfer state from O^{2-} to Eu^{3+}. The second band, with a maximum at about 455 nm, is assigned to the self-activated luminescence of the host matrix. The emission spectrum obtained under excitation at 394 nm exhibits the transitions $^5D_0 \rightarrow {}^7F_{0,1,2,3,4}$ of Eu^{3+}(Fig. 6a, solid line). Strong emission peaks observed at 580–598 nm ($^5D_0 \rightarrow {}^7F_1$) and 605–627 nm ($^5D_0 \rightarrow {}^7F_2$) are assigned to the magnetic and electric dipole transitions, respectively. It is well known that the intensity ratio of these emission peaks indicates the symmetry of the local site where the europium ion is embedded [41–44].

The transition $^5D_0 \rightarrow {}^7F_2$, which is sensitive to the coordination environment, has a higher intensity than the non-sensitive $^5D_0 \rightarrow {}^7F_1$ transition. This intensity difference strongly indicates that Eu^{3+} ions occupy a low symmetry site without an inversion center. The presence of the strongly forbidden $^5D_0 \rightarrow {}^7F_0$ transition supports this statement [45,46].

The excitation spectrum of $La_{0.93}Tb_{0.07}PO_4$ was obtained by monitoring emission at 542 nm (Fig. 6b, dashed line). The observed sharp peaks are assigned to the 4f–4f transitions of Tb^{3+}. The strongest one located at 376 nm corresponds to the $^7F_6 \rightarrow {}^5G_6$, $^5D_3$ transitions. The emission spectrum obtained under excitation at 376 nm is shown in Fig. 6b (solid line). Four narrow and intense peaks corresponding to the characteristic transitions of Tb^{3+} ($^5D_4 \rightarrow {}^7F_{6,5,4,3}$) can be easily identified [47–49]. The $^5D_4 \rightarrow {}^7F_{2,1}$ and $^5D_4 \rightarrow {}^7F_0$ transitions also appear as low-intensity peaks at around 646 and 675 nm, respectively. Furthermore, this sample shows a broadband at 390–500 nm with a maximum at 437 nm, assigned to the self-activated luminescence of the host matrix.

Fig. 6c clearly depicts the occurrence of the self-activated luminescence of $LaPO_4$. A broad band with a maximum at about 384 nm dominates the excitation spectrum (dashed line). However, due to the large band gap of 6.4 eV (194 nm) in the monoclinic $LaPO_4$ structure [50], the existence of intermediate bands or localized levels in the forbidden zone (band gap) is possible, what has been previously reported in Eu^{3+}/Li^+ co-doped phosphates [51,52]. The emission spectrum (solid line) shows a blue-greenish broad band with a maximum at around 480 nm under excitation at 400 nm. The intermediate bands in the gap region of the host ($LaPO_4$) are related to the matrix interaction with adsorbed species (CO_3^{2-}, H_2O) or a capping agent (EG) [51]. It is also possible that $CO_2^{\cdot-}$ radicals resulted from the bond cleavage of EG during the synthesis are trapped within the formed lattice or interstitial positions, which results in the formation of luminescent centers [53,54]. This phenomenon would give rise of photoluminescence with a short lifetime through a strong electron–photon coupling [55].

Tunable luminescent properties may be conferred to inorganic host matrices by co-doping with different lanthanide ions. It is also possible to control these properties by varying the concentration of a dopant or the excitation wavelength. Fig. 7 shows excitation spectra of Eu^{3+}/Tb^{3+} co-doped $LaPO_4$ with different lanthanide concentrations. By monitoring the $^5D_0 \rightarrow {}^7F_2$ transition of Eu^{3+} at 615 nm, the spectra reveal the characteristic transitions of terbium, as well as the intense $^7F_0 \rightarrow {}^5L_6$ transition of europium. These results indicate the efficient energy transfer from Tb^{3+} to Eu^{3+}, but not from Eu^{3+} to Tb^{3+}.

The emission spectra of the co-doped samples under excitation at 255, 376 and 394 nm, together with the decay curves, are displayed in Fig. 8. In all spectra, a broad blue emission band assigned to the self-activated luminescence of the matrix can be observed. Furthermore, under excitation at 394 nm (Fig. 8a), the spectra illustrate sharp emission peaks of Eu^{3+} corresponding to the $^5D_0 \rightarrow {}^7F_{0,1,2,3,4}$ transitions. Comparing Fig. 8b and c, the emission peaks of both Tb^{3+} and Eu^{3+} ions can be visible, which confirms the energy transfer from Tb^{3+} to Eu^{3+}. It is worth noting that, under excitation at 255 nm, the $La_{0.93}Eu_{0.017}Tb_{0.053}PO_4$ and $La_{0.93}Eu_{0.011}Tb_{0.059}PO_4$ samples have almost identical spectra, with the $^5D_4 \rightarrow {}^7F_5$ transition of Tb^{3+} of low-intensity compared to emission peaks of Eu^{3+}.

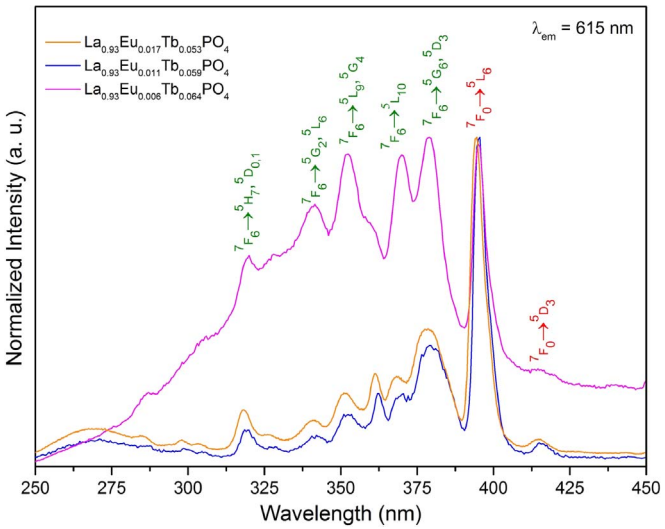

Fig. 7. PL excitation spectra of $La_{0.93}Eu_{0.017}Tb_{0.053}PO_4$, $La_{0.93}Eu_{0.011}Tb_{0.059}PO_4$ and $La_{0.93}Eu_{0.006}Tb_{0.064}PO_4$.

However, as we can see from the spectrum of $La_{0.93}Eu_{0.006}Tb_{0.064}PO_4$, the intensity of the $^5D_4 \rightarrow {}^7F_5$ transition increases as terbium and europium concentration grows and decreases, respectively, indicating that the energy transfer from the Tb^{3+} to Eu^{3+} ions is very efficient.

The luminescent decay curves of co-doped samples were recorded (Fig. 8d). All curves were fitted by using a bi-exponential decay equation:

$$I(t) = A_1 \exp^{(-t/\tau 1)} + A_2 \exp^{(-t/\tau 2)} \quad (1)$$

where I is the luminescence intensity at time t, A_1 and A_2 are the fitting constants, and τ_1 and τ_2 are the short- and long-decay exponential components, respectively. In addition, the average lifetimes (τ_{av}) were calculated by using Eq. (2), and the values are presented in Table 1.

$$\tau_{av} = (A_1\tau_1^2 + A_2\tau_2^2)/(A_1\tau_1 + A_2\tau_2) \quad (2)$$

A bi-exponential decay suggests that lanthanide ions are allocated in two different environments. However, there is only one kind of lattice site in the $LaPO_4$ structure, normally occupied by La, where europium and terbium ions can be embedded. Therefore, the observed lifetimes τ_1 and τ_2 are most probably related to lanthanide ions on a surface and in the core of particles, respectively [51]. Furthermore, it should be mentioned that the surface contribution to the lifetime becomes meaningful only for small particles where the content of atoms at the surface is comparable to that in the core. This statement is supported by TEM results, which display mesostructures formed by agglomerates of seed crystals with extremely small size.

By inspecting data in Table 1, it appears that lifetimes measured by monitoring emission at 615 nm increase with increasing Eu^{3+} content reaching a maximum value and then decrease. When the $^5D_4 \rightarrow {}^7F_5$ transition of Tb^{3+} is monitored (542 nm), lifetimes decrease with increasing europium content, which may confirm the efficient energy transfer from Tb^{3+} to Eu^{3+} ions [56].

Fig. 9 presents the energy level diagrams of the Tb^{3+} and Eu^{3+} ions in the $LaPO_4$ host matrix, as well as the proposed energy transfer process. The excitation process occurs from the ground state of terbium $4f^8$ ($^7F_6$) to the excited state $^5D_3$ upon UV light irradiation (376 nm). Subsequently, the electron decays to the lower-localized terbium excited state $^5D_4$ via multiphonon relaxation (MR). Then, the electron returns to the ground state, generating the terbium emissions ($^5D_4 \rightarrow {}^7F_{6,5,4}$) or transfers this energy to excited energy levels of Eu^{3+} by cross-relaxation followed by the relaxation to the emissive $^5D_0$ (Eu^{3+}) level. Finally, radiative decays from $^5D_0$ (Eu^{3+}) level to $^7F_{0-4}$

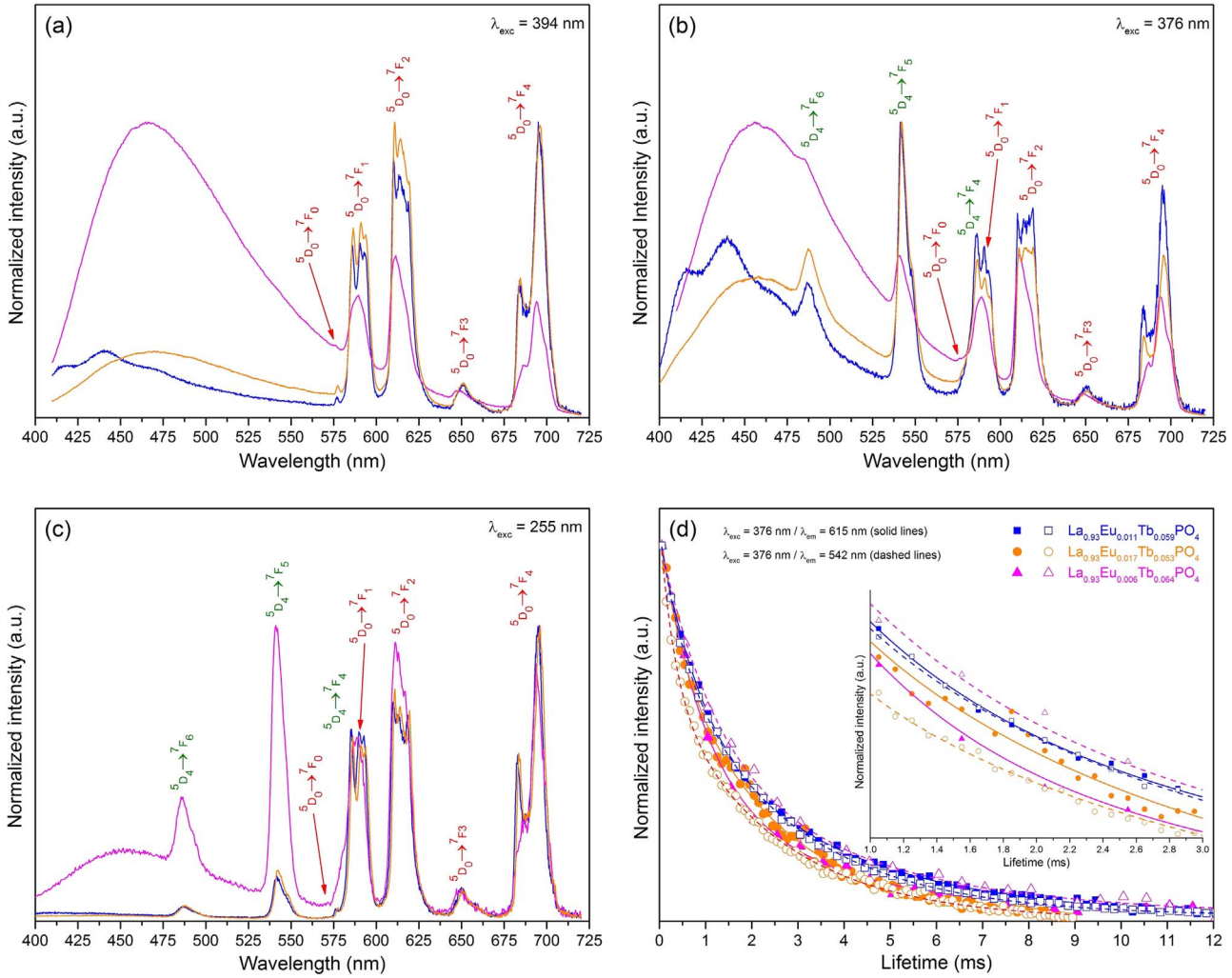

Fig. 8. PL emission spectra, λ_{exc}=394 nm (a), 376 nm (b), 255 nm (c) and the luminescence decay curves of the co-doped samples (d).

Table 1
Short- and long-decay exponential components and the average lifetimes.

Sample	λ_{em} (nm)	τ_1 (ms)	τ_2 (ms)	τ_{av} (ms)
$La_{0.93}Eu_{0.006}Tb_{0.064}PO_4$	615	0.61289	2.03149	1.57853
$La_{0.93}Eu_{0.011}Tb_{0.059}PO_4$	615	2.59430	0.64129	2.20484
$La_{0.93}Eu_{0.017}Tb_{0.053}PO_4$	615	1.58828	0.27712	1.51203
$La_{0.93}Eu_{0.006}Tb_{0.064}PO_4$	542	0.82181	2.70502	2.17676
$La_{0.93}Eu_{0.011}Tb_{0.059}PO_4$	542	1.83361	0.38316	1.71454
$La_{0.93}Eu_{0.017}Tb_{0.053}PO_4$	542	0.22376	1.64601	1.52778

levels give rise to the orange-red emissions.

It is known that, in general, the transfer of energy between lanthanide ions is nonradiative, which occurs through dipole-dipole or electric dipole-quadrupole interactions. In this process, there is no emission or absorption of photons, but there is an energy transfer (ET) from the donor to the acceptor level by the interaction of electronic clouds of the species.

As can be seen from the emission spectra, the photoluminescent properties of prepared powders are strongly dependent on the type and concentration of dopants, which affect not only the emission intensity but also their color. To study the effects of the dopant species and their concentration on the color of the photoluminescent emissions, the chromatic coordinates (CIE 1931 and field of view 2 degrees) were calculated by using the program SPECTRA LUX [57].

Fig. 10 shows the CIE diagram, pointing out the colors exhibited by the synthesized samples. These results reveal that the luminescent

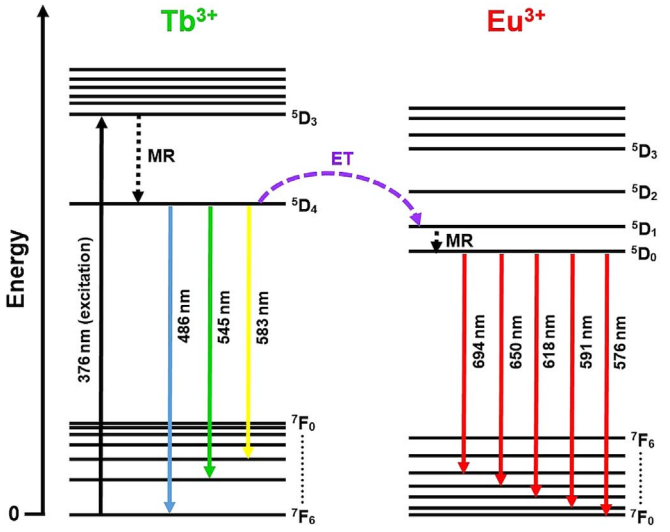

Fig. 9. Energy level diagrams of Tb^{3+} and Eu^{3+} ions in the $LaPO_4$ host matrix and the related energy transfer process.

properties of the studied system may be tuned and the color control can be achieved by changing both the Eu^{3+}/Tb^{3+} molar ratio and the excitation wavelength. It seems possible to tune the color between blue-greenish and red, and probably to reach the white.

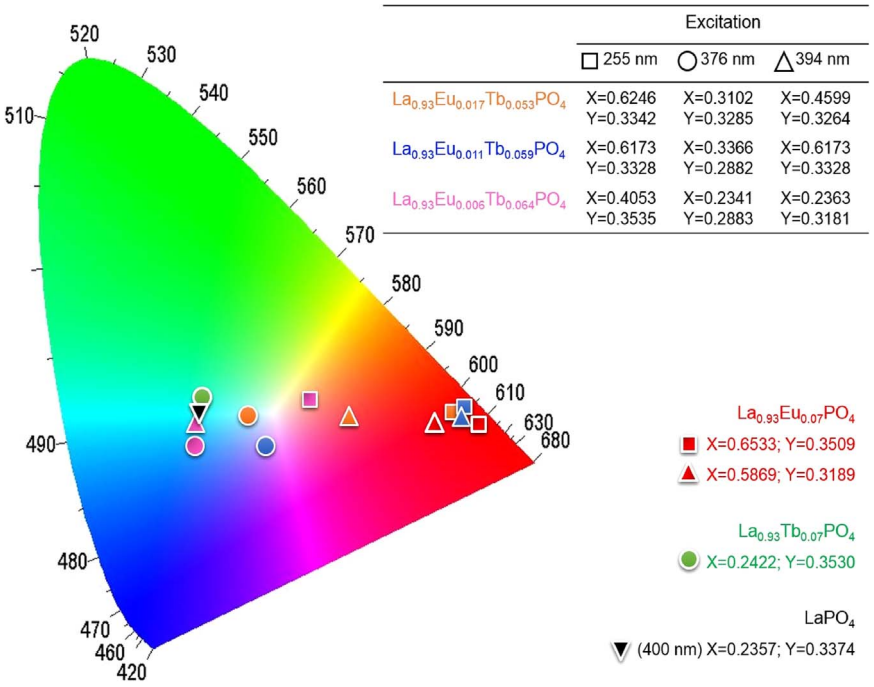

Fig. 10. Chromaticity diagram and color coordinates of synthesized powders.

The combination of all factors, such as the possibility of color tuning, small particle size, and simplicity of the synthetic route used, indicates the high viability of these materials in biomedicine, more specifically, in the field of labeling and sensing.

4. Conclusions

In summary, we have presented the fast approach, using microwave-assisted heating and ethylene glycol, for the synthesis of nanostructured $LaPO_4:Eu^{3+}/Tb^{3+}$. The analysis by X-ray diffraction and electron microscopy indicated the rapid nucleation of seed crystals with the monoclinic unit cell, which posteriorly self-assemble, forming nanostructured aggregates.

It was noted that the post-calcination step at 600 °C led to the formation of nanoparticles with a size of around 25 nm. A photoluminescence with tunable color properties was achieved, and it was found to be dependent on the Eu^{3+}/Tb^{3+} molar ratio and the excitation wavelength. The chromatic coordinates suggest that the color observed can be tuned from red to blue-greenish and even to white due to the blue self-activated luminescence originating from intermediate bands in the gap region. The results reveal that these materials exhibit interesting morphological and optical properties, which opens a large window for advanced applications such as biolabeling and sensing.

Acknowledgments

The authors thank Dr. Raquel Milani and CETENE for the TEM analysis as well as the Brazilian agencies CAPES and CNPq for their financial support. This work was supported by PRONEX/FACEPE/CNPq (Grant no. APQ-0675- 1.06/14).

References

[1] P. Huang, W. Zheng, S. Zhou, D. Tu, Z. Chen, H. Zhu, R. Li, En Ma, M. Huang, X. Chen, Lanthanide-doped $LiLuF_4$ upconversion nanoprobes for the detection of disease biomarkers, Angew. Chem. Int. Ed. 53 (2014) 1252–1257.
[2] E. Hemmer, N. Venkatachalam, H. Hyodo, A. Hattori, Y. Ebina, H. Kishimoto, K. Soga, Upconverting and NIR emitting rare earth based nanostructures for NIR-bioimaging, Nanoscale 5 (2013) 11339–11361.
[3] P.C.S. Filho, O.A. Serra, Red, green, and blue lanthanum phosphate phosphors obtained via surfactant-controlled hydrothermal synthesis, J. Lumin. 129 (2009) 1664–1668.
[4] S. Yang, D.L. Han, M. Gao, J.H. Yang, Bayanheshig, Controllable morphology and tunable colors of Mg and Eu ion co-doped ZnO by thermal annealing, Cryst. Eng. Comm. 16 (2014) 6896–6900.
[5] B.S. Barros, A.C. de Lima, Z.R. da Silva, D.M.A. Melo, S. Alves-Jr, Synthesis and photoluminescent behavior of Eu^{3+}-doped alkaline-earth tungstates, J. Phys. Chem. Solids 73 (2012) 635–640.
[6] A.S.S. de Camargo, L.A.O. Nunes, J.F. Silva, A.C.F.M. Costa, B.S. Barros, J.E.C. Silva, G.F. de Sá, S. Alves Jr, Efficient green and red upconversion emissions in Er^{3+}/Yb^{3+} co-doped $ZnAl_2O_4$ phosphor obtained by combustion reaction, J. Phys. Condens. Matter 19 (2007) 1–7.
[7] Z. Lu, L. Chena, Y. Tangb, Y. Li, Preparation and luminescence properties of Eu^{3+}-doped $MSnO_3$ (M=Ca, Sr and Ba) perovskite materials, J. Alloy. Compd. 387 (2005) L1–L4.
[8] Y. Wanga, T. Endo, E. Xiec, D. He, B. Liu, Luminescence properties of $Ca_4GdO(BO_3)_3$:Eu in ultraviolet and vacuum ultraviolet regions, Microelectron. J. 35 (2004) 357–361.
[9] A. Watras, R. Pazik, P.J. Dereń, Optical properties of Ce^{3+} doped ABO_3 perovskites (A=La, Gd, Y and B=Al, Ga, Sc), J. Lumin. 133 (2013) 35–38.
[10] H. Ji, Z. Huang, Z. Xia, M.S. Molokeev, X. Jiang, Z. Lin, V.V. Atuchin, Comparative investigations of the crystal structure and photoluminescence property of eulytite-type $Ba_3Eu(PO_4)_3$ and $Sr_3Eu(PO_4)_3$, Dalton Trans. 44 (2015) 7679–7686.
[11] C.S. Lim, A. Aleksandrovsky, M. Molokeev, A. Oreshonkov, V. Atuchin, The modulated structure and frequency upconversion properties of $CaLa_2(MoO_4)_4:Ho^{3+}/Yb^{3+}$ phosphors prepared by microwave synthesis, Phys. Chem. Chem. Phys. 17 (2015) 19278–19287.
[12] V.V. Atuchin, N.F. Beisel, E.N. Galashov, E.M. Mandrik, M.S. Molokeev, A.P. Yelisseyev, A.A. Yusuf, Z. Xia, Pressure-stimulated synthesis and luminescence properties of microcrystalline $(Lu,Y)_3Al_5O_{12}:Ce^{3+}$ garnet phosphors, ACS Appl. Mater. Interfaces 7 (2015) 26235–26243.
[13] X. He, J. Gao, S.S. Gambhir, Z. Cheng, Near-infrared fluorescent nanoprobes for cancer molecular imaging: status and challenges, Trends Mol. Med. 16 (2010) 574–583.
[14] D. Che, X. Zhu, P. Liu, Y. Duan, H. Wang, Q. Zhang, Y. Li, A facile aqueous strategy for the synthesis of high-brightness $LaPO_4$:Eu nanocrystals via controlling the nucleation and growth process, J. Lumin. 153 (2014) 369–374.
[15] Z. Fu, W. Bu, High efficiency green-luminescent $LaPO_4$:Ce, Tb hierarchical nanostructures: synthesis, characterization, and luminescence properties, Solid State Sci. 10 (2008) 1062–1067.
[16] U. Rambabu, N.R. Munirathnam, T.L. Prakash, S. Buddhudu, Emission spectra of $LnPO_4:RE^{3+}$(Ln=La, Gd; RE=Eu, Tb and Ce) powder phosphors, Mater. Chem. Phys. 78 (2002) 160–169.
[17] Na Niu, P. Yang, Y. Wang, W. Wang, F. He, S. Gai, D. Wang, $LaPO_4:Eu^{3+}$, $LaPO_4:Ce^{3+}$, and $LaPO_4:Ce^{3+},Tb^{3+}$ nanocrystals: oleic acid assisted solvothermal synthesis, characterization, and luminescent properties, J. Alloy. Compd. 509 (2011) 3096–3102.
[18] C. Buezea, I.I.P. Blandino, K. Robbie, Nanomaterials and nanoparticles: sources and toxicity, Biointerphases 2 (2007) MR17–MR172.
[19] A. Paulraj, P. Natarajan, K. Munnisamy, M.K. Nagoor, K.P. Nattar, B. Abdulrazak, J. Duraisamy, Photoluminescence efficiencies of nanocrystalline versus bulk

Y_2O_3:Eu phosphor—revisited, J. Am. Ceram. Soc. 94 (2011) 1627–1633.
[20] B. Damien, A. Fabienne, C. Thibault, S. Dimitri, B.A. Didier, Solid-state synthesis of monazite-type compounds $LnPO_4$ (Ln=La–Gd), Solid State Sci. 9 (2007) 432–439.
[21] H. Meyssamy, K. Riwotzki, A. Kornowski, S. Naused, M. Haase, Wet-Chemical Synthesis of Doped Colloidal Nanomaterials: particles and Fibers of $LaPO_4$:Eu, $LaPO_4$:Ce, and $LaPO_4$:Ce, Tb, Adv. Mater. 11 (1999) 840–844.
[22] G. Rui, Q. Dong, L. Wei, Sol-gel synthesis and photoluminescence of $LaPO_4$:Eu^{3+} nanorods, Trans. Nonferrous Met. Soc. China 20 (2010) 432–436.
[23] S. Gallini, J.R. Jurado, M.T. Colomer, Combustion synthesis of nanometric powders of $LaPO_4$ and Sr-substituted $LaPO_4$, Chem. Mater. 17 (2005) 4154–4161.
[24] M. Ferhi, K. Horchani-Naifer, M. Férid, Hydrothermal synthesis and photoluminescence of the monophosphate $LaPO_4$:Eu (5%), J. Lumin. 128 (2008) 1777–1782.
[25] K. Manickathai, S.K. Viswanathan, M. Alagar, Synthesis and characterization of CdO and CdS nanoparticles, Indian J. Pure Appl. Phys. 46 (2008) 561–564.
[26] K.G. Sharma, N.R. Singh, Synthesis of $CaWO_4$:Eu^{3+} phosphor powders via ethylene glycol route and its optical properties, J. Rare Earths 30 (2012) 310–314.
[27] C.S. Lim, A. Aleksandrovsky, M. Molokeev, A. Oreshonkov, V. Atuchin, Microwave sol–gel synthesis and upconversion photoluminescence properties of $CaGd_2(WO_4)_4$:Er^{3+}/Yb^{3+} phosphors with incommensurately modulated structure, J. Solid State Chem. 228 (2015) 160–166.
[28] C.S. Lim, V.V. Atuchin, A.S. Aleksandrovsky, M.S. Molokeev, Preparation of $NaSrLa(WO_4)_3$:Ho^{3+}/Yb^{3+} ternary tungstates and their upconversion photoluminescence properties, Mater. Lett. 181 (2016) 38–41.
[29] C.R. Patra, G. Alexandra, S. Patra, D.S. Jacob, A. Gedanken, A. Landau, Y. Gofer, Microwave approach for the synthesis of rhabdophane-type lanthanide orthophosphate (Ln=La, Ce, Nd, Sm, Eu, Gd and Tb) nanorods under solvothermal conditions, New J. Chem. 29 (2005) 733–739.
[30] S. Grazulis, D. Chateigner, R.T. Downs, A.T. Yokochi, M. Quiros, L. Lutterotti, E. Manakova, J. Butkus, P. Moeck, A. Le Bail, Crystallography open database – an open-access collection of crystal structures, J. Appl. Cryst. 42 (2009) 726–729.
[31] C. Cheng, F. Xu, H. Gu, Facile synthesis and morphology evolution of magnetic iron oxide nanoparticles in different polyol processes, New J. Chem. 35 (2011) 1072–1079.
[32] M.A.v. Huis, L.T. Kunneman, K. Overgaag, Q. Xu, G. Pandraud, H.W. Zandbergen, D. Vanmaekelbergh, Low-temperature nanocrystal unification through rotations and relaxations probed by in situ transmission electron microscopy, Nano Lett. 11 (2008) 3959–3963.
[33] R.Q. Song, H. Colfen, Mesocrystals—ordered nanoparticle superstructures, Adv. Mater. 22 (2010) 1301–1330.
[34] H. Colfen, M. Antonietti, Mesocrystals: inorganic superstructures made by highly parallel crystallization and controlled alignment, Angew. Chem., Int. Ed. 44 (2005) 5576–5591.
[35] J.A.D. Guillén, A.F. Fuentes, S. Gallini, M.T. Colomer, A rapid method to obtain nanometric particles of rhabdophane $LaPO_4.nH_2O$ by mechanical milling, J. Alloy. Compd. 427 (2007) 87–93.
[36] Y. Yang, Synthesis and luminescent properties of $LaPO_4$:Eu^{3+} microspheres, Mater. Sci. Eng. B 178 (2013) 807–810.
[37] A. Hezel, S.D. Ross, Forbidden transitions in the infra-red spectra of tetrahedral anions-III, Spectra-structure correlations in perchlorates, sulphates and phosphates of the formula MXO_4, Spectrochim. Acta 22 (1966) 1949–1961.
[38] D. Eisenberg, W. Kauzmann, The Structure and Properties of Water, Oxford University Press, London, 1969, pp. 228–245.
[39] J.J. Max, C. Chapados, Isotope effects in liquid water by infrared spectroscopy. III. H2O and D2O spectra from 6000 to 0 cm^{-1}, J. Chem. Phys. 131 (2009) 184505.
[40] K. Krishnan, R.S. Krishnan, Raman and infrared spectra of ethylene glycol, Proc. Indian Acad. Sci. Chem. Sci. 30 (1996) 111–122.
[41] N.S. Baek, Y.H. Kim, D.H. Lee, K.D. Seo, H.K. Kim, Effect of coordination environment on the photophysical properties of luminescent Europium (III) complexes, Bull. Korean Chem. Soc. 30 (2009) 1553–1558.
[42] V.V. Atuchin, A.S. Aleksandrovsky, O.D. Chimitova, T.A. Gavrilova, A.S. Krylov, M.S. Molokeev, A.S. Oreshonkov, B.G. Bazarovand, J.G. Bazarova, Synthesis and spectroscopic properties of monoclinic α-$Eu_2(MoO_4)_3$, J. Phys. Chem. C 118 (2014) 15404–15411.
[43] P. Shi, Z. Xia, M.S. Molokeev, V.V. Atuchin, Crystal chemistry and luminescence properties of red-emitting $CsGd_{1-x}Eu_x(MoO_4)_2$ solid-solution phosphors, Dalton Trans. 43 (2014) 9669–9676.
[44] F. Cheng, Z. Xia, M.S. Molokeev, X. Jing, Effects of composition modulation on the luminescence properties of Eu^{3+} doped $Li_{1-x}Ag_xLu(MoO_4)_2$ solid-solution phosphors, Dalton Trans. 44 (2015) 18078–18089.
[45] B.S. Barros, R.S. de Oliveira, J. Kulesza, V.R.M. Melo, D.M.A. Melo, S.A. Reddish-orange Jr, Ca3-xAl2O6:xEu^{3+} nanophosphors: fast synthesis and photophysical properties, J. Phys. Chem. Solids 78 (2015) 90–94.
[46] B. Chen, J. Yu, X. Liang, $LaAlO_3$ hollow spheres: synthesis and luminescence properties, Langmuir 27 (2011) 11654–11659.
[47] V.V. Atuchin, A.S. Aleksandrovsky, O.D. Chimitova, A.S. Krylov, M.S. Molokeev, B.G. Bazarov, J.G. Bazarova, Zhiguo Xia, Synthesis and spectroscopic properties of multiferroic β′-$Tb_2(MoO_4)_3$, Opt. Mater. 36 (2014) 1631–1635.
[48] F. Baur, F. Glocker, T. Jüstel, Photoluminescence and energy transfer rates and efficiencies in Eu^{3+} activated $Tb_2Mo_3O_{12}$, J. Mater. Chem. C 3 (2015) 2054–2064.
[49] M. Chen, Z. Xia, M.S. Molokeev, Q. Liu, Morphology and phase transformation from $NaCaSiO_3OH$ to $Na_2Ca_2Si_2O_7$ and photoluminescence evolution via Eu^{3+}/Tb^{3+}doping, Chem. Commun. 52 (2016) 11292–11295.
[50] S.V. Syrotyuk, Y.M. Chornodolskyy, V.V. Vistovskyy, A.S. Voloshinovskii, A.V. Gektin, Band structure of $LaPO_4$, Funct. Mater. 20 (2013) 373–377.
[51] A.K. Parchur, A.I. Prasad, S.B. Rai, R. Tewari, R.K. Sahu, Observation of intermediate bands in Eu^{3+} doped YPO_4 host: Li^+ ion effect and blue to pink light emitter, AIP Adv. 2 (2012) 032119.
[52] L. Li, Y. Su, G. Li, Chemical modifications of red phosphor $LaPO_4$:Eu^{3+} nanorods to generate white light, J. Mater. Chem. 20 (2010) 459–465.
[53] P.P. Yang, P. Yang, X. Teng, J. Lin, L. Huang, A novel luminescent mesoporous silica/apatite composite for controlled drug release, J. Mater. Chem. 21 (2011) 5505–5510.
[54] C.M. Zhang, J. Yang, Z.W. Quan, P.P. Yang, C.X. Li, Z.Y. Hou, J. Lin, Hydroxyapatite nano- and microcrystals with multiform morphologies: controllable synthesis and luminescence properties, Cryst. Growth Des. 9 (2009) 2725–2733.
[55] C. Zhang, J. Lin, Defect-related luminescent materials: synthesis, emission properties and applications, Chem. Soc. Rev. 41 (2012) 7938–7961.
[56] Z. Fu, X. Wang, Y. Yang, Z. Wu, D. Duan, X. Fu, Hydrothermal synthesis, electronic structure and tunable luminescence of single-phase $Ca_5(PO_4)_3F$:Tb^{3+}, Eu^{3+} microrods†, Dalton Trans. 43 (2014) 2819–2827.
[57] P.A. Santa-Cruz, F.S. Teles, Spectra lux software, Ponto Quântico Nanodispositivos/RENAMI 10 (2003).